The Astrophysical Journal Letters, 999:L22 (11pp), 2026 March 1 https://doi.org/10.3847/2041-8213/ae45a3

A Protoplanet Candidate in the PDS 66 Disk Indicated by Silicon Sulfide Isotopologues

Tomohiro C. Yoshida[1,12], Felipe Alarcón[2,12], Jaehan Bae[3], Myriam Benisty[4], Kiyoaki Doi[4], Stefano Facchini[2], Charles J. Law[5,13], Hideko Nomura[1,6], Laura Perez[7], Giovanni Rosotti[2], Yuhito Shibaike[8], Richard Teague[9], Takashi Tsukagoshi[10], and Yoshihide Yamato[11]
[1] National Astronomical Observatory of Japan, 2-21-1 Osawa, Mitaka, Tokyo 181-8588, Japan; tomohiroyoshida.astro@gmail.com
[2] Dipartimento di Fisica, Università degli Studi di Milano, Via Celoria 16, 20133 Milano, Italy; felipe.alarcon@unimi.it
[3] Department of Astronomy, University of Florida, Gainesville, FL 32611, USA
[4] Max-Planck Institute for Astronomy (MPIA), Königstuhl 17, 69117 Heidelberg, Germany
[5] Department of Astronomy, University of Virginia, Charlottesville, VA 22904, USA
[6] Department of Astronomical Science, The Graduate University for Advanced Studies, SOKENDAI, 2-21-1 Osawa, Mitaka, Tokyo 181-8588, Japan
[7] Departamento de Astronomía, Universidad de Chile, Camino El Observatorio 1515, Las Condes, Santiago, Chile
[8] Graduate School of Science and Engineering, Kagoshima University, 1–21–35 Korimoto, Kagoshima City, Kagoshima 890–0065, Japan
[9] Department of Earth, Atmospheric, and Planetary Sciences, Massachusetts Institute of Technology, Cambridge, MA 02139, USA
[10] Faculty of Engineering, Ashikaga University, Ohmae 268-1, Ashikaga, Tochigi, 326-8558, Japan
[11] RIKEN Pioneering Research Institute, 2-1 Hirosawa, Wako, Saitama 351-0198, Japan
Received 2025 December 3; revised 2026 February 2; accepted 2026 February 12; published 2026 February 27

Abstract

Despite observational progress in planet formation, the stage in which planetesimals grow into planets remains poorly understood. During this phase, protoplanets may develop gaseous envelopes that are warmer than the surrounding disk gas, potentially providing observable signatures through molecules otherwise depleted in cold regions. In this Letter, we report the detection of the silicon sulfide isotopologues ^{28}SiS $J = 16-15$ and ^{30}SiS $J = 18-17$ in the protoplanetary disk around PDS 66 (MP Mus) at a significance of $\sim 5\sigma-6\sigma$, using the Atacama Large Millimeter/submillimeter Array. These constitute the second and first detections of ^{28}SiS and ^{30}SiS in a protoplanetary disk, respectively. The emission appears as a compact source at $r = 60$ au in the southwestern region of the disk, unresolved with a $\sim 0\farcs5$ beam, and shows a velocity consistent with Keplerian rotation, suggesting a protoplanetary origin. By modeling the line fluxes, we constrain the emitting radius to $\sim 0.5-4$ au and estimate a SiS mass of 10^{22}–10^{23} g, corresponding to at least $\sim 10\%$ of the silicon contained in local dust grains. Because complete sublimation of a substantial fraction of dust grains by local processes is difficult to achieve, this result instead implies an accumulation of silicon from a larger region. We propose that a circumplanetary envelope surrounding a low-mass protoplanet, where pebble accretion and subsequent sublimation of grains may enhance gaseous silicon abundance with respect to observable dust grains around it, can account for the observed characteristics.

Unified Astronomy Thesaurus concepts: Protoplanetary disks (1300); Planet formation (1241); Astrochemistry (75)

1. Introduction

Planet formation is a process in which small dust grains grow into planets within protoplanetary disks (e.g., J. Drążkowska et al. 2023). In the initial stage, micron-sized dust grains undergo collisional growth and accumulate into relatively large particles, or pebbles. These pebbles may further evolve into planetesimals, potentially through the streaming instability (A. N. Youdin & J. Goodman 2005). The planetesimals then accrete other planetesimals or pebbles under the presence of aerodynamic drag from the disk gas, allowing them to grow to the sizes of terrestrial planets or the cores of giant planets (C. W. Ormel & H. H. Klahr 2010; M. Lambrechts & A. Johansen 2012). Once the cores become sufficiently massive, they can accrete disk gas through circumplanetary disks. Recent observational studies have revealed that these evolutionary stages are indeed occurring. Dust evolution in disks has been recognized as a variation in the continuum spectral index at millimeter wavelengths (e.g., L. Testi et al. 2014; A. Miotello et al. 2023). Radial dust accumulation is a necessary condition for the streaming instability and has been suggested by high-resolution Atacama Large Millimeter/submillimeter Array (ALMA) observations (e.g., S. M. Andrews et al. 2018). Relatively massive protoplanets undergoing gas accretion have been directly detected (e.g., M. Keppler et al. 2018; S. Y. Haffert et al. 2019), together with their circumplanetary disks (e.g., M. Benisty et al. 2021). Additionally, gas kinematics traced by molecular/atomic lines (e.g., C. Pinte et al. 2018; R. Teague et al. 2019; F. Alarcón et al. 2022) and spatially localized, excess line emission (e.g., J. Bae et al. 2022; A. S. Booth et al. 2023; C. J. Law et al. 2023) also suggest the presence of embedded giant planets.

However, the evolutionary pathway from planetesimals to massive ($\sim 1 M_{\rm Jup}$) protoplanets remains poorly constrained from an observational perspective. This is due at least in part to the fact that the masses of these nascent planets are much less than that of a Jupiter as they are initially forming/evolving. It is therefore important to identify observational signatures that can probe this intermediate stage. In the

[12] These authors contributed equally to this work.
[13] NASA Hubble Fellowship Program Sagan Fellow.

presence of disk gas, planetesimals or small protoplanets can acquire envelopes (e.g., J. Szulágyi et al. 2016). Such envelopes extend out to the Hill (or Bondi) radius, which reaches ∼1 au for an Earth-sized planet located at 100 au from the central star. This implies that a circumplanetary envelope at the outer regions of disks can attain a size that can be probed with high-resolution observations.

Within such circumplanetary envelopes, significant heating processes may occur. In the context of pebble accretion, pebbles accreted onto an envelope surrounding relatively massive cores ($\sim 1\,M_{\oplus}$) may evaporate before reaching the core, thereby limiting core growth (M. G. Brouwers et al. 2018). The sublimated or thermally processed material may later recondense as the protoplanet cools or may be recycled into the protoplanetary disk (M. G. Brouwers et al. 2018; Y. Wang et al. 2023). Although it remains uncertain which species can most effectively trace these evolutionary stages, promising candidates include molecules that are strongly depleted in cold disk environments but released or formed in relatively heated and/or shocked environments, such as silicon-bearing molecules (L. I. Cleeves et al. 2015; C. J. Law et al. 2023; L. Keyte et al. 2024; A. J. Cridland et al. 2025).

In this Letter, we report the detection of two silicon sulfide (SiS) isotopologues, ^{28}Si^{32}S and ^{30}Si^{32}S, at a distance of ∼60 au from the central star in the protoplanetary disk around PDS 66 (MP Mus). The PDS 66 disk is among the nearest protoplanetary disks to Earth, at a distance of $d = 97.9$ pc (Gaia Collaboration et al. 2021). The central star is a K1V-type star (E. E. Mamajek et al. 2002), with estimated mass, luminosity, age, and mass accretion rate of $M_{\star} \simeq 1.28\,M_{\odot}$, $L_{\star} \simeq 1.2\,L_{\odot}$, 7–10 Myr, and $1.3 \times 10^{-10}\,M_{\odot}\,\mathrm{yr}^{-1}$, respectively (L. Ingleby et al. 2013; Á. Ribas et al. 2023; A. F. Izquierdo et al. 2025). The disk has been imaged at infrared and millimeter wavelengths. The near-infrared (H-band) image shows a gap-like structure at a radius of ∼60 au from the central star (S. G. Wolff et al. 2016; H. Avenhaus et al. 2018). High-resolution (4 au) ALMA Band 6 ($\lambda \sim 1.3$ mm) observations reveal that the continuum disk extends to ∼60 au in radius with no detected substructure (Á. Ribas et al. 2023). A lack of substantial substructures in high-resolution observations is relatively uncommon in large disks (J. Bae et al. 2023), although follow-up studies have revealed shallow substructures (A. Aguayo et al. 2025; Á. Ribas et al. 2025). An upper limit of $\sim 1 M_{\mathrm{Jup}}$ on planets in the outer disk regions has been placed based on CO channel maps (C. Pinte et al. 2025).

The structure of this Letter is as follows: Section 2 describes the observations and results, Section 3 presents the interpretations and discussion, and Section 4 summarizes the conclusions.

2. Observations and Results

2.1. Observations

We observed the ^{28}Si^{32}S $J = 16-15$ and ^{30}Si^{32}S $J = 18-17$ pure rotational transitions toward the PDS 66 disk. Hereafter we omit the atomic number 32 for the main sulfur isotopologue. The two lines were observed by different ALMA programs (^{28}SiS: #2023.1.00334.S, PI: L. Trapman; ^{30}SiS: #2023.1.00525.S, PI: T. C. Yoshida).

^{28}Si is the most abundant stable isotope of silicon, while ^{30}Si is the least abundant. The solar isotope ratio of ^{28}Si/^{30}Si is estimated to be 30.1 (M. Asplund et al. 2021). Table 1 lists the spectroscopic parameters of the observed lines. We provide two rest frequencies from the CDMS (H. S. P. Müller et al. 2005) and JPL (H. M. Pickett et al. 1998) databases. The CDMS and JPL entries adopt different molecular constants based on H. S. P. Müller et al. (2007) and F. J. Lovas & E. Tiemann (1974), respectively. Unless otherwise noted, we use the constants on the CDMS catalog in this work.

Details of the observations and data reduction are described in Appendix A. In summary, we produced two image cubes for the ^{28}SiS $J = 16-15$ transition, one with a narrow channel width of $\Delta v = 1.25\,\mathrm{km\,s^{-1}}$ and another with a wider channel width of $5.0\,\mathrm{km\,s^{-1}}$ to maximize the signal-to-noise ratio (S/N) of a potentially broad line. For the ^{30}SiS $J = 18-17$ transition, only the narrow-channel cube was generated. The resulting beam sizes and noise levels are summarized in Table 1. Channel maps of the narrow-channel data cubes are presented in Appendix A.

2.2. Detection of SiS Isotopologues

We detected significant emission in both image cubes. In the $v_{\mathrm{LSR}} = 5\,\mathrm{km\,s^{-1}}$ channel of the wide-channel ^{28}SiS $J = 16-15$ cube, we found $\sim 5\sigma$ emission in the southwestern part of the disk. In the $v_{\mathrm{LSR}} = 3.75\,\mathrm{km\,s^{-1}}$ channel of the ^{30}SiS $J = 18-17$ cube, a $\sim 6\sigma$ signal was detected at a similar position. This is the first detection of ^{30}SiS in protoplanetary disks. Figure 1 shows the S/N channel maps for both lines, and Appendix A.4 presents the pixel-value histograms. The sources are spatially unresolved and have position angles consistent with the synthesized beam, indicating that the emission originates from a point source at the current spatial resolution (∼0.″5). The upper-state energies of those lines are >100 K, which is significantly higher than the expected temperature at this region from the stellar luminosity (∼17 K; Appendix B).

After we specified the disk center by fitting a Gaussian to the corresponding continuum images, we measured the relative position of the emission peaks with respect to the disk center as (ΔR.A., Δdecl.) = (−0.″51, −0.″55) and (−0.″31, −0.″47) for the ^{28}SiS $J = 16-15$ and ^{30}SiS $J = 18-17$ lines, respectively. The separation between the two positions is ∼0.″21. According to the ALMA Technical Handbook (P. Cortes et al. 2025), the 1σ relative astrometric accuracy for sources with these S/Ns is ∼0.″17, indicating that the apparent offset is consistent with the statistical error.

Figure 1 also compares the SiS emission with the 338 GHz continuum[14] (P. Curone et al. 2025) and H-band polarized-intensity image (H. Avenhaus et al. 2018). Dotted ellipses indicate $r = 60$ au, corresponding to the outer radius of the millimeter-continuum disk (Á. Ribas et al. 2023). The detected point source lies near the disk edge and within the infrared gap. An azimuthally averaged radial profile analysis of the continuum disk suggests a more extended structure up to $r \sim 70$ au (P. Curone et al. 2025), which is shown in dashed ellipses in Figure 1 and slightly beyond the SiS emission region. In addition, interestingly, the SiS emission is colocated with the azimuthal brightness drop in the H- and $K1$-band image with Gemini Planet Imager (S. G. Wolff et al. 2016). They attributed this to a shadow cast by material in the inner region or cold stellar spots. Note that, however,

[14] The continuum image was obtained from the exoALMA repository on the Harvard Dataverse (P. Curone 2025). Note that the image frequency (338 GHz) differs slightly from the one used in the original paper (332 GHz).

Table 1
Observed SiS Isotopologue Transitions

Transition	CDMS Freq. (GHz)	JPL Freq. (GHz)	E_{up} (K)	$g_u A_{ul}$ (10^{-2} s^{-1})	Beam Size (P.A.)	rms (mJy beam^{-1})	Int. Flux (mJy km s^{-1})
^{28}SiS $J = 16-15$	290.3808	290.3803	118	1.37	$0\farcs62 \times 0\farcs42$ (35°)	1.1	21 ± 4
^{30}SiS $J = 18-17$	315.0625	315.0659	144	1.97	$0\farcs57 \times 0\farcs41$ (−6°)	1.7	12 ± 2

Note. The rms values are measured for images with a channel width of 1.25 km s^{-1}.

H. Avenhaus et al. (2018) did not find this structure in their *H*-band image with Very Large Telescope/SPHERE. To summarize the comparison of radial locations, we also plot the deprojected radial profiles of the 338 GHz continuum (P. Curone et al. 2025) and *H*-band polarized intensity (weighted by r^2; H. Avenhaus et al. 2018) with the radial location of the SiS source obtained by weighted average of the positions of the two isotopologues (Figure 2).

Figure 3 presents the spectra at the pixels where the emission peaks. In the narrow-channel ^{28}SiS $J = 16-15$ cube, $\sim 3\sigma-4\sigma$ signals appear over five channels around $v_{LSR} \sim 5$ km s^{-1}, implying a line width of $\sim$5 km s^{-1} (FWHM). This corresponds to the $\sim 5\sigma$ detection in the wide-channel cube shown in the second panel. For the ^{30}SiS $J = 18-17$ line, the signal appears only at $v_{LSR} = 3.75$ km s^{-1} and is not spectrally resolved at a velocity resolution of $\sim$1 km s^{-1}. Although the S/N is low, we found that the two lines have potentially different line widths, which we discuss in Appendix B. The integrated flux densities are 21 ± 4 and 12 ± 2 mJy km s^{-1} for the ^{28}SiS $J = 16-15$ and ^{30}SiS $J = 18-17$ lines, respectively.

The systemic velocity of PDS 66 has been measured as $v_{LSR} \simeq 3.98$ km s^{-1} from CO observations (Á. Ribas et al. 2023; A. F. Izquierdo et al. 2025). The line-of-sight Keplerian velocity within the beam of the compact source ranges between $v_{LSR} = 4$ and 6 km s^{-1}. Thus, the ^{28}SiS $J = 16-15$ source is consistent with the local Keplerian velocity, while the ^{30}SiS $J = 18-17$ source appears slightly offset. However, this is likely within the uncertainty of the rest frequency (Appendix C). Overall, the SiS emission is both astrometrically and spectrally consistent with the PDS 66 system, strongly suggesting an association with the disk. While consistent proper motion between the emission and the disk (or the star itself) would further strengthen this scenario, the two observations were conducted only 7 months apart. The expected stellar proper motion during this window is $\sim$38 mas (Gaia Collaboration et al. 2021), which is insufficient to provide a definitive constraint. Nevertheless, a background or foreground origin is unlikely for the following reasons. Potential sources with previous SiS detections, such as AGB stars (e.g., N. A. Patel et al. 2011; T. Danilovich et al. 2019), massive protostellar environments (e.g., B. Tercero et al. 2011; K. E. I. Tanaka et al. 2020; A. Ginsburg et al. 2023), or protostellar outflows (e.g., L. Podio et al. 2017), typically exhibit strong continuum emission around them, which is not observed here. For example, AGB stars at 130–2200 pc have millimeter fluxes of 3–70 mJy (T. Danilovich et al. 2025), and the carbon star IRC+10216 at 135 pc, where SiS isotopologues are detected, shows $\sim$650 mJy (N. A. Patel et al. 2011). The detection of ^{28}SiS in the protoplanetary disk around HD 169142 (C. J. Law et al. 2023) further supports the interpretation that the SiS emission originates in situ from the PDS 66 system.

2.3. Derived Physical Quantities

The detection of the rare isotopologue ^{30}SiS indicates that the total SiS mass is substantial. To quantify the physical conditions of the source, we modeled the integrated flux densities of the detected lines under the assumptions of local thermal equilibrium, a homogeneous cylindrical emitting region with radius R, and an isotopologue ratio ^{28}SiS/^{30}SiS = 30 (M. Asplund et al. 2021). Spectroscopic parameters were taken from the CDMS database (H. S. P. Müller et al. 2005, 2007), and integrated line fluxes were computed over a grid of temperatures T, SiS column densities N_{SiS}, and emitting radii R.

In our model, the integrated flux of each transition was computed as

$$F_i = \pi R_a^2 \int_{-\infty}^{\infty} B_{\nu_i}(T)\,(1 - e^{-\tau_i(v)})\,dv, \quad (1)$$

where i denotes each line, R_a is the apparent radius corresponding to a physical radius R at a distance of 98 pc, ν_i is the frequency of the transition, $B_{\nu_i}(T)$ is the Planck function, and $\tau_i(v)$ is the optical depth as a function of velocity offset from the line center. We compared F_i with the measured values and identified combinations of (N_{SiS}, R, T) that reproduce both integrated fluxes within the 1σ uncertainties.

Parameter sets consistent with the observations are shown in Figure 4. For T = 100–2000 K, the SiS column density increases from $\sim 10^{16}$ to 10^{19} cm^{-2}, while the emitting radius decreases from $\sim$4 to 0.5 au. The corresponding SiS mass is $M_{SiS} \sim 10^{22}$–10^{23} g. As expected from the observed flux ratio, the ^{28}SiS $J = 16-15$ line is highly optically thick, with peak optical depths of 30–200, which constrains the emitting radius. In contrast, the ^{30}SiS $J = 18-17$ line is roughly 30 times less optically thick and is therefore still sensitive to the column density. Caveats associated with these calculations are discussed in Appendix B.

3. Discussion

3.1. Dust Mass Inferred from SiS and Continuum

In general, silicon-bearing molecules are highly locked in the solid phase of protoplanetary disks, namely, dust grains. Therefore, the detection of SiS indicates a dynamically active environment in the disk, even a possible protoplanetary origin. The main reservoir of silicon in dust grains is expected to be silicates forming the grain cores, such as Mg_2SiO_4, which may constitute $\sim$33% of the total dust mass (e.g., J. B. Pollack et al. 1994; T. Birnstiel et al. 2018). A few percent of the silicon may also reside in the grain mantles, potentially as SiO, as suggested by observations of protostellar outflows (A. Gusdorf et al. 2008). Releasing silicon from the grain core requires significant heating (>1000 K) or strong shocks, although the condition is much less stringent for grain mantles.

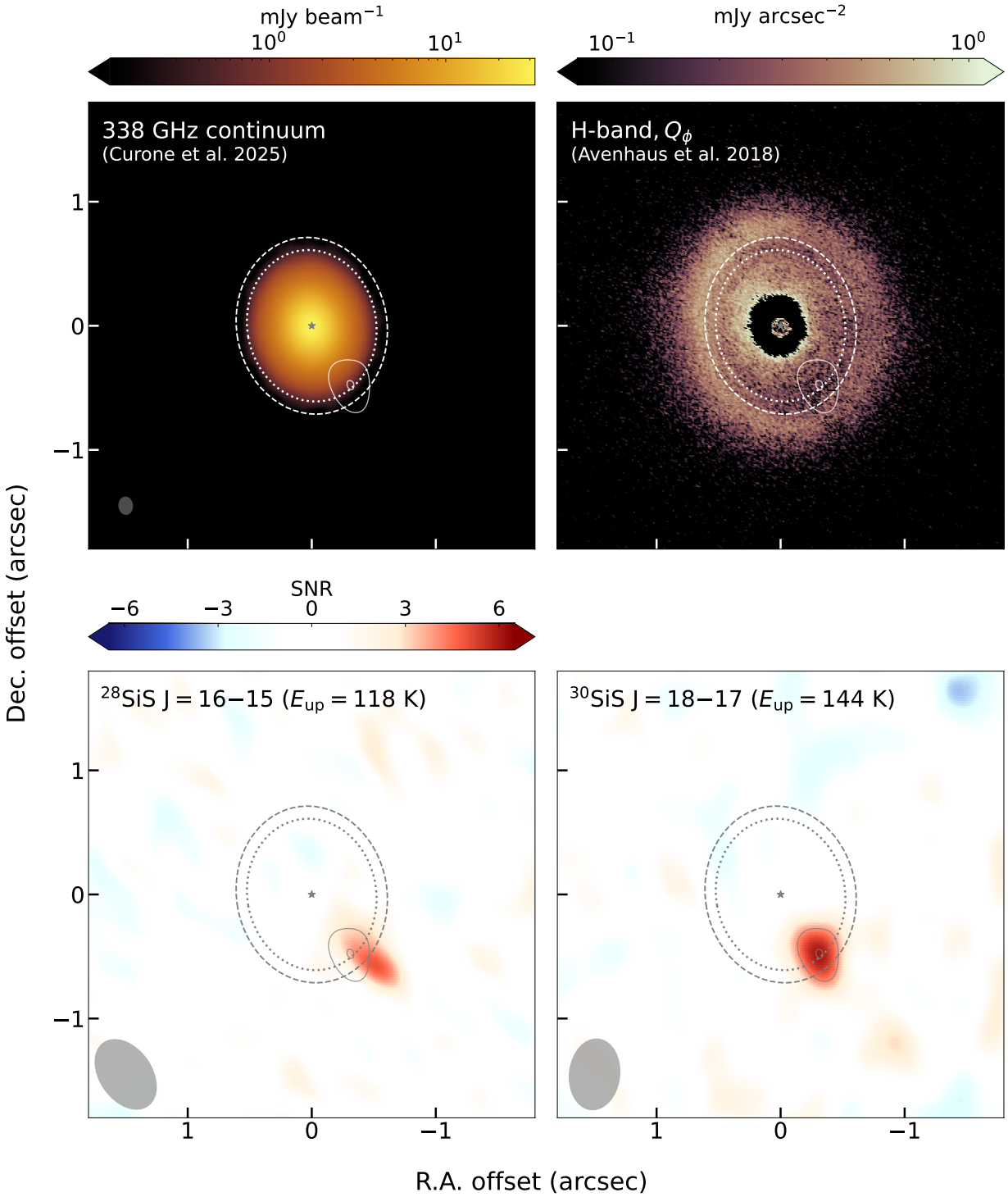

Figure 1. Top panels: 338 GHz continuum image (P. Curone et al. 2025) and Q_ϕ image in the H band (H. Avenhaus et al. 2018). Bottom panels: S/N maps of the ^{28}SiS $J = 16-15$ and ^{30}SiS $J = 18-17$ lines at channels that cover $v_{LSR} \simeq 2.5-7.5$ km s^{-1} and $3.1-4.4$ km s^{-1}, respectively, where the emission peaks. Note that there might be uncertainty in the rest frequency adopted here (Appendix C). In all panels, the dotted and dashed ellipses indicate radii of $r = 60$ and 70 au, respectively, corresponding roughly to the edge of the millimeter-continuum disk (Á. Ribas et al. 2023; P. Curone et al. 2025). Contours show the 3σ and 6σ levels of the ^{30}SiS $J = 18-17$ line, and the apparent shift between two lines can be explained by statistical error of astrometry (Section 2.2). The star symbol marks the position of the central star, and the gray ellipse in the lower left corner represents the synthesized beam (except for the H-band image).

Once released into the gas phase, gas-phase reactions with S-bearing molecules are proposed to form SiS molecules (M. Rosi et al. 2018; A. Zanchet et al. 2018; M. A. M. Paiva et al. 2020; V. C. Mota et al. 2021; R. C. Fortenberry & B. A. McGuire 2024; E. Mendoza et al. 2024).

In any case, the silicon detected in SiS should originate from dust grains. Assuming that the fraction of silicon released from one dust grain is χ ($\chi \simeq 1$ if the entire grain is sublimated, while $\chi \lesssim 0.1$ if only the mantle contributes), the corresponding dust mass needed to account for silicon in SiS can be

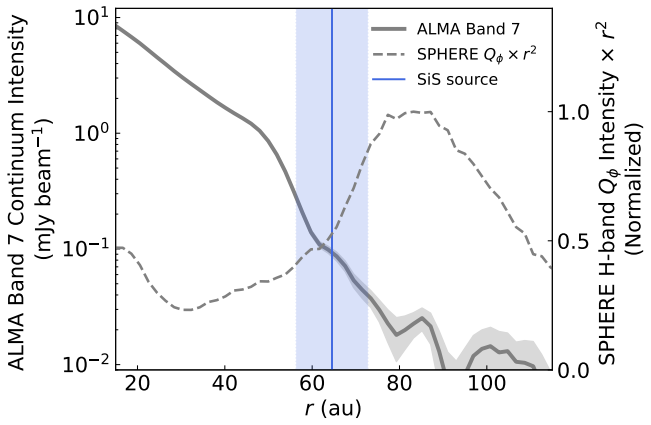

Figure 2. Radial location of the SiS source with the radial profiles of the 332 GHz continuum and H-band Q_ϕ emission multiplied by r^2 (H. Avenhaus et al. 2018; P. Curone et al. 2025). Note that the SiS source location is an averaged value of the two isotopologues weighted by their astrometric uncertainties. The blue shaded region shows the 1σ uncertainty of the averaged location.

estimated as

$$M_{d,\,\mathrm{SiS}} \sim 15\chi^{-1}M_{\mathrm{SiS}} \quad (2)$$

$$\sim(10^{-5} - 10^{-4})\,\chi^{-1}\,M_\oplus \quad (3)$$

$$\sim(0.1 - 1)\,\chi^{-1}\,M_{\mathrm{Ceres}} \quad (4)$$

for $T = 100$–2000 K using the results in Section 2.3. Here the factor of $\sim$15 is the mass ratio of the dust mass to Si, assuming that Si is dominated by silicate that is five times heavier than Si and has a mass fraction of $\sim$33% of one grain. This indicates that even if the silicon originates from sublimation of dust grain cores, at least $10^{-5}\,M_\oplus$ of dust is required. Moreover, if the silicon comes only from grain mantles, an even larger dust mass is necessary.

We compare the dust mass needed to account for the SiS, $M_{d,\,\mathrm{SiS}}$, with continuum observations. First, we assume that dust grains are uniformly distributed within the SiS-emitting region, with a radius of $\sim$0.4–5 au, and the surface brightness matches that of the surrounding azimuthal region. The 332 GHz continuum intensity at $r = 60$ au is estimated as $I_{\mathrm{cont}} \sim 6 \times 10^8\,\mathrm{Jy\,Sr^{-1}}$ by P. Curone et al. (2025) using `frankenstein` fitting (J. Jennings et al. 2020). Assuming the millimeter opacity of a typical protoplanetary disk dust mixture, $\kappa = 3.5\,\mathrm{cm^2\,g^{-1}}$ (T. Birnstiel et al. 2018), and a temperature equal to that of SiS, the dust mass within radius R is

$$\frac{\pi R^2 I_{\mathrm{cont}}}{\kappa B_\nu(T)} \sim 10^{-6}\ \mathrm{to}\ 10^{-3}\,M_\oplus, \quad (5)$$

depending on the assumed temperature ($T = 10^2$–10^3 K).

However, the azimuthally and radially localized SiS emission may also suggest a corresponding localized dust excess. Although previous sensitive millimeter-continuum ALMA observations reveal no point-source excess at the SiS location (Á. Ribas et al. 2023; P. Curone et al. 2025; Á. Ribas et al. 2025), we estimate the 3σ upper limit of the excess dust mass using the continuum noise level ($\sigma \sim 25\ \mu$Jy at 332 GHz; P. Curone et al. 2025) via

$$\frac{3\sigma d^2}{\kappa B_\nu(T)} \sim 10^{-4}\ \mathrm{to}\ 10^{-3}\,M_\oplus. \quad (6)$$

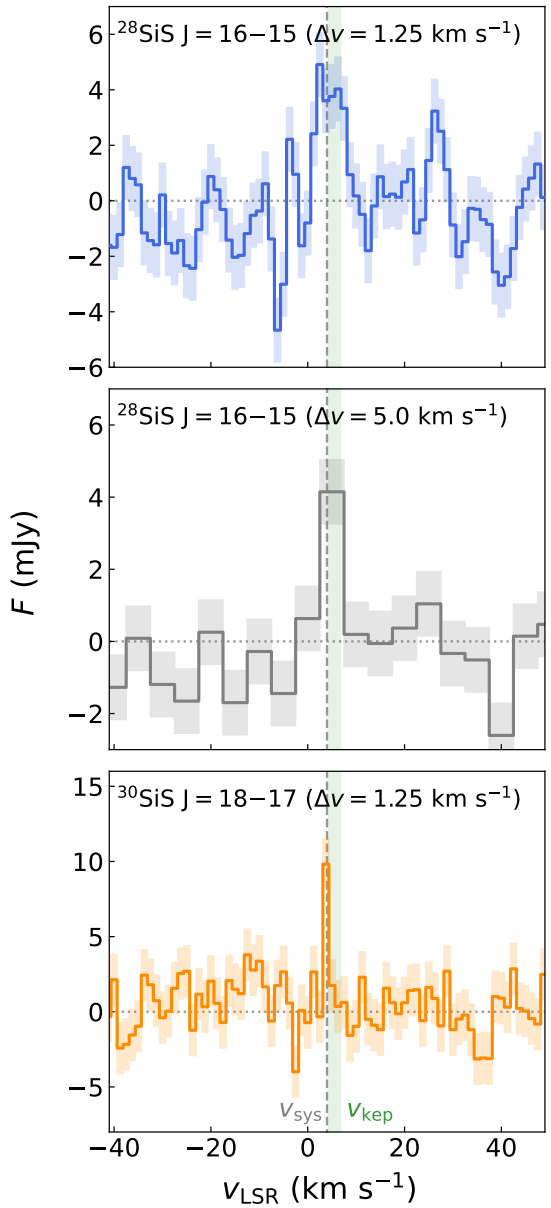

Figure 3. Spectra of the ^{28}SiS $J = 16$–15 and ^{30}SiS $J = 18$–17 lines extracted at the peak S/N positions (Figure 1). The top and bottom panels show spectra from the narrow channel width cubes, while the middle panel corresponds to the wide-channel ^{28}SiS $J = 16$–15 cube. The shaded regions indicate 1σ noise levels. The vertical dashed line marks the systemic velocity, and the green band represents the range of projected Keplerian velocities within one beam.

Figure 5 shows these dust mass estimates from the background intensity and point-source upper limit as a function of assumed temperature. Interestingly, the dust masses inferred from continuum observations are roughly comparable to the dust mass required to supply the observed SiS. At $T \sim 100$ K, at least $\sim$10% (and likely more) of the local dust grains must have sublimated. At $T > 1000$ K, the silicon content in the local dust grains under the point-source assumption reaches the total SiS silicon, implying that all dust grains in this region may have sublimated. In summary, we find that if the SiS originates from a local process in a closed system, the silicate dust cores at this location must have been almost completely sublimated.

Alternatively, silicon may have been accumulated at this position relative to the amount of dust grains. In this case,

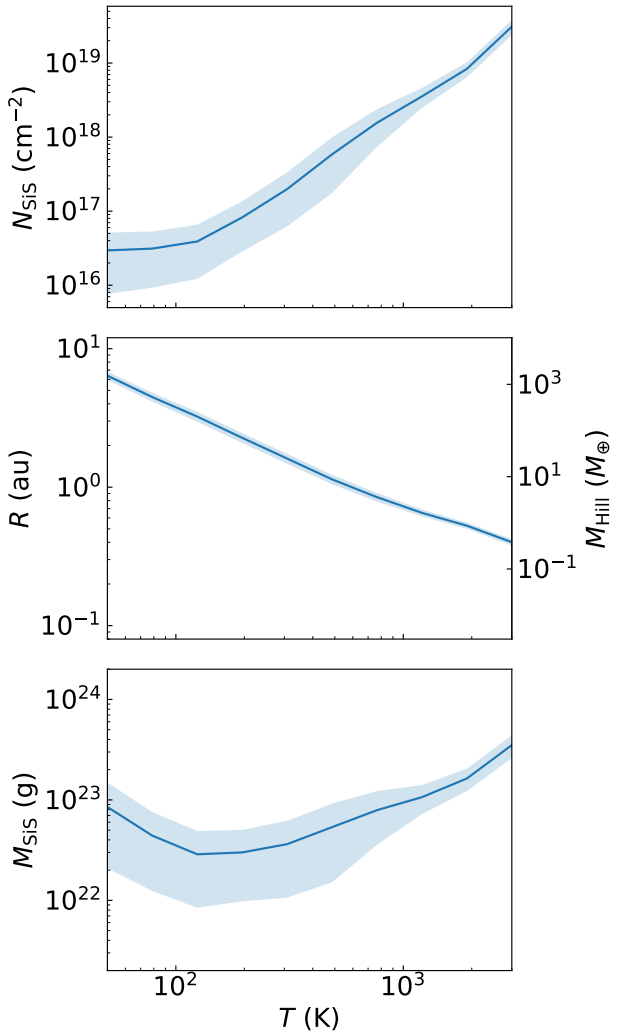

Figure 4. Derived SiS column densities (N_{SiS}) and emitting radii (R) as a function of the assumed temperature. The bottom panel shows the SiS mass (M_{SiS}). For the middle panel (R), we also plot the planet's mass assuming that the emitting radius is equal to the Hill radius (see Section 3.2.4).

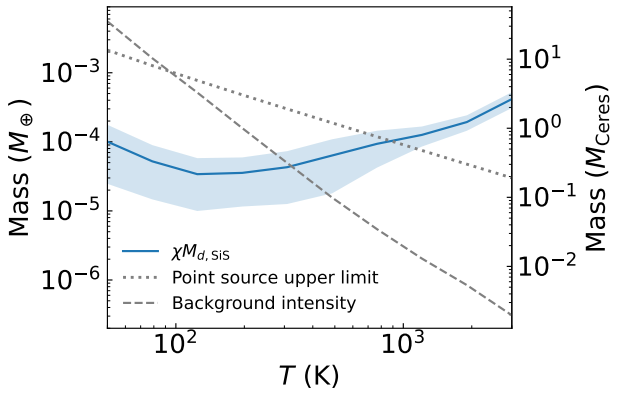

Figure 5. Dust mass required to supply gas-phase SiS compared with dust masses inferred from background continuum intensity and the upper limit from a potential point source. χ is the fraction of silicon released from one dust grain.

release from grain mantles alone could also suffice if the degree of accumulation is substantial. Such an enhancement can be divided into two nonexclusive possibilities: silicon could be selectively concentrated at the location, and/or the dust grains traced at millimeter wavelengths could be selectively depleted. The latter case would correspond to conversion of dust grains to larger bodies such as planetesimals. It is noteworthy that although our discussion has so far focused on silicon rather than sulfur, a gas enriched in silicon would be also expected to be sulfur-rich because sulfur is generally more volatile than silicon. Indeed, S-bearing molecules have been routinely detected in warm Herbig disks, while Si-bearing molecules are not (e.g., A. S. Booth et al. 2025; F. Zagaria et al. 2025). In the following section, we consider four phenomena that are potentially consistent with the above discussion.

3.2. Possible Origin of SiS

3.2.1. Planetary-driven Outflow

Another detection of SiS in a protoplanetary disk has been reported in HD 169142 (C. J. Law et al. 2023). However, its characteristics differ from PDS 66; the emission is extended rather than a point source, and it is spectrally offset by $\sim$6 km s^{-1} from the local Keplerian rotation. In that case, the emission was attributed to a polar outflow driven by the massive protoplanet candidate HD 169142 b (e.g., A. C. Quillen & D. E. Trilling 1998; F. Alarcón et al. 2022; I. Hammond et al. 2023; L. Keyte et al. 2024; T. C. Yoshida et al. 2024). SiS could be released directly from the dust grains by strong shocks or formed via gas-phase reactions of Si and other species after release from the grain mantles (e.g., M. Rosi et al. 2018; M. A. M. Paiva et al. 2020; V. C. Mota et al. 2021; R. C. Fortenberry & B. A. McGuire 2024; E. Mendoza et al. 2024).

Nevertheless, a planet-driven outflow is unlikely to account for the emission in PDS 66. The detected velocity is consistent with the local Keplerian speed, and the emission is compact, with an inferred spatial scale of $\sim$0.4–5 au. These characteristics suggest that the SiS originates from a component that is gravitationally bound to the potential planet rather than an outflow. It also remains unclear whether an outflow could supply the large local fraction of silicon required relative to the silicon contained in the local dust grains.

3.2.2. Circumplanetary Disk

Another possibility is that the SiS emission originates from a hot region in a circumplanetary disk, where dust grains can be thermally evaporated. However, Y. Shibaike & C. Mordasini (2024) showed that even in the circumplanetary disk around the giant planet PDS 70 c, temperatures exceeding $\sim 10^3$ K, which is needed to thermally sublimate silicate, occur only in the very inner region, within $\sim$0.1 au. This implies that most silicate in the disk should remain solid, which is inconsistent with the observations. Still, as an analogy of young stellar objects (e.g., J. Bae et al. 2014), a potential outburst of the protoplanet could sufficiently heat the grains across large regions of the circumplanetary disk. A lower temperature could also release the silicon from the dust mantles; however, it is unknown whether there is any mechanism that can selectively deplete dust grains or enhance gas-phase silicon.

3.2.3. Transient Events

Some transient events could lead to the sublimation of dust grains or larger bodies. For example, giant impacts can

vaporize a substantial amount of material (e.g., S. J. Lock & S. T. Stewart 2017), which could be consistent with the mass fractions, as such giant bodies cannot be observed. However, the duration of such events would be typically very short, so the probability of observing one by chance is low, making this scenario less likely than the others. Future observations could test this possibility because such emission should show time variability.

3.2.4. Circumplanetary Envelope

A circumplanetary envelope may form around a relatively low mass planet, with a typical spatial scale set by the Hill (or Bondi) radius. During this stage, pebble accretion, a promising process for forming planetary cores, can operate (e.g., M. Lambrechts & A. Johansen 2012). If the protoplanet is relatively massive ($\sim 1\,M_\oplus$), rocky pebbles cannot reach the core but instead sublimate within the envelope, a process referred to as "ablation" (e.g., M. G. Brouwers et al. 2018). This process limits direct core growth and enriches the envelope with silicate vapor (e.g., M. G. Brouwers et al. 2018; M.-L. Steinmeyer et al. 2023; M.-L. Steinmeyer & A. Johansen 2024). For example, M.-L. Steinmeyer & A. Johansen (2024) found that envelopes become saturated by SiO vapor for planet masses exceeding $0.6\,M_\oplus$, although their calculations assumed equilibrium chemistry and a protoplanet at 1 au. We note that silicon contained in grain mantles has not been considered in this context, and such silicon may be released more easily into the gas phase at lower temperatures.

In the middle panel of Figure 4, we plot the planet's mass assuming that the inferred emitting radius is equal to the Hill radius: $M_{\rm Hill} = 3(R/60\,{\rm au})^3 M_\star$. This suggests that the emitting radius is broadly consistent with the Hill radius of a 0.1–10 $M_\oplus$ planet at $r = 60$ au, 0.26–1.2 au. $M_{d,\,\rm SiS}$ (Equation (2)) corresponds to $(10^{-6}$ to $10^{-3})\chi^{-1}$ of these masses. These low planet masses may also be consistent with the substructure-less disk (Á. Ribas et al. 2023; C. Pinte et al. 2025), although there is a gap in the infrared image (H. Avenhaus et al. 2018). However, note that the masses would be lower than a typical range to exhibit an observable gap in scattered-light images (R. Dong & J. Fung 2017), potentially implying a different origin of the gap, such as a shadow (Á. Ribas et al. 2023).

We estimate the pebble accretion rate at this location. The pebble accretion rate in the two-dimensional regime can be roughly estimated as

$$\dot{M}_{\rm PA} \sim \sqrt{GM_p {\rm St}}\, H_g r^2 \Sigma_d, \tag{7}$$

where H_g is the gas scale height, Σ_d is the dust surface density, M_p is the planet mass, and St is the Stokes number (e.g., C. W. Ormel 2024). We adopt Equation (B1) for H_g and assume ${\rm St} = 0.1$ for simplicity. P. Curone et al. (2025) measured the 332 GHz continuum intensity at $r = 60$ au (just outside the disk edge) to be $I_{\rm cont} \sim 6 \times 10^8\,{\rm Jy\,Sr^{-1}}$ using `frankenstein` fitting (J. Jennings et al. 2020). Assuming a dust opacity of $\kappa = 3.5\,{\rm cm^2\,g^{-1}}$ (T. Birnstiel et al. 2018) and optically thin emission, the dust surface density is estimated as

$$\Sigma_d = \frac{I_{\rm cont}}{\kappa B_\nu(T_{\rm mid})} \sim 5 \times 10^{-3}\,{\rm g\,cm^{-2}}. \tag{8}$$

Using Equation (7), the pebble accretion rate for $M_p = 0.1$–$10\,M_\oplus$ is estimated to be $\dot{M}_{\rm PA} \sim 4 \times 10^{-7}$ to $4 \times 10^{-6}\,M_\oplus\,{\rm yr^{-1}}$.

This rate implies that the dust mass of $(10^{-5}$ to $10^{-4})\chi^{-1}\,M_\oplus$ can be supplied within $\sim$(1–100)χ^{-1} yr by pebble accretion, far shorter than not only the typical disk lifetime but also the orbital timescale. We also note that planetesimal accretion onto the envelope may contribute to silicate vaporization (C. Valletta & R. Helled 2019).

The detailed mechanisms remain uncertain and are beyond the scope of this Letter. Nevertheless, the observed SiS mass can be explained by the pebble accretion rate and an internal process in which only a very small fraction of the accreted dust grains are processed and their silicon is retained in the envelope.

3.3. Consistency with Nondetections of CO and SiO

The SiS emission might suggest potential detections of other molecular lines. For example, CO is a well-known tracer of molecular gas and has been observed by the exoALMA project (R. Teague et al. 2025). However, the CO channel maps presented by C. Pinte et al. (2025) do not show a counterpart of the SiS emission. This is naturally explained if this emission is being absorbed by the optically thick protoplanetary disk gas above it, even if CO originates from the same source as SiS. We note that this would not be the case if the two CO-emitting layers could be clearly distinguished in channel maps (e.g., J. Bae et al. 2022), which is, however, not the case for the PDS 66 disk (M. Galloway-Sprietsma et al. 2025; C. Pinte et al. 2025).

SiO lines are another potential tracer, as they are sensitive to regions with strong shocks or heating (e.g., A. Gusdorf et al. 2008; M. K. McClure et al. 2025). We searched the ALMA archive for all SiO $v = 0$ transitions with velocity resolution better than $\sim$20 km s^{-1} and found that project ID # 2017.1.01687.S (PI: A. Ribas) observed the SiO $J = 3$–2 line ($E_{\rm up} = 13$ K) at 130.2687 GHz. The observations were published by Á. Ribas et al. (2023), and we refer to their paper for the observational details. We obtained a pipeline-calibrated dataset from the National Radio Astronomy Observatory archive and concatenated the provided measurement sets. After subtracting the continuum emission, we created image cubes with velocity widths of 1.25 and 5 km s^{-1} using natural weighting. No significant emission was detected, and we place a 3σ upper limit on the integrated intensity of 3.8 mJy km s^{-1} based on the narrow-channel cube. Assuming the same R and T for SiO as for SiS, the corresponding upper limit on the SiO column density is estimated to be 10^{15}–10^{18} g cm^{-2}, resulting in a lower limit of the SiS/SiO ratio of 5–60. The high SiS/SiO ratio may reflect that SiS formation routes such as Si + SH → SiS + H (V. C. Mota et al. 2021) efficiently work.

Meanwhile, in AGB stars, where both SiS and SiO are routinely detected, the SiS/SiO ratio ranges from 0.05 to 20 (F. L. Schöier et al. 2007). Notably, carbon stars typically have SiS/SiO > 1, while O-rich M-type stars have SiS/SiO < 1, reflecting the influence of the photospheric C/O ratio (I. Cherchneff 2006). Although the chemistry in AGB stars may not directly apply to the PDS 66 system, the high SiS/SiO ratio may suggest C/O > 1.

In protoplanetary disks, the C/O ratio is often higher than unity (e.g., E. A. Bergin et al. 2016; A. D. Bosman et al. 2021). Indeed, Á. Ribas et al. (2023) detected hydrocarbons in the PDS 66 disk, suggesting an enhanced C/O, although the exact

value is currently unclear. A likely mechanism to enhance C/O is removal of water ice by radial drift of icy grains (S. Krijt et al. 2020). In the context of the PDS 66 disk, the lack of substructure suggests active radial drift (Á. Ribas et al. 2023; A. Aguayo et al. 2025), providing a consistent picture where C/O is enhanced. More locally, the C/O ratio in a protoplanetary envelope could be enhanced by selective removal of water ice during pebble accretion (Y. Wang et al. 2023), which is directly related to the mechanism discussed in Section 3.2.4. Since the C/O ratio is a key parameter linking planet formation and exoplanet compositions (K. I. Öberg et al. 2011; N. Madhusudhan et al. 2017), future observations and chemical modeling of the SiS source are crucial.

4. Summary

In this Letter, we presented observations of the ^{28}SiS and ^{30}SiS lines in the protoplanetary disk around PDS 66. Our main results are summarized as follows:

1. The ^{28}SiS $J = 16-15$ and ^{30}SiS $J = 18-17$ lines are detected at $r = 60$ au in the southwestern region of the disk. These constitute the second and first detections of ^{28}SiS and ^{30}SiS, respectively, in protoplanetary disks. Both lines are spatially and spectrally colocated within uncertainties. The source is unresolved, located at the edge of the millimeter-continuum disk and within the infrared gap, and its velocity is consistent with Keplerian rotation, suggesting a connection to planet formation processes.
2. Modeling of the line fluxes constrains the column densities and emitting radius as a function of temperature. The detection of ^{30}SiS implies a SiS mass of $10^{22}-10^{23}$ g. The emitting radius derived from the optically thick main isotopologue emission is 0.5–4 au.
3. The large fraction of silicon in SiS relative to the silicon inferred from dust grains at the same location indicates that if the silicon originates from in situ processing of dust, complete sublimation of dust grain cores would be required. Alternatively, if silicon is locally accumulated relative to dust grains, sublimation of grain mantles alone would suffice.
4. We propose a circumplanetary envelope around a low-mass ($<10\,M_\oplus$) protoplanet as a plausible explanation. Pebble accretion may supply silicon to the envelope through sublimation of grain cores and/or mantles. The high SiS/SiO ratio implied by the nondetection of SiO would be further related to an elevated C/O ratio in the planet-forming material if the chemistry in the envelope is similar to that of carbon stars.

The next step is to characterize the physical properties and molecular abundances of the source with higher spatial and spectral resolution observations. A dedicated line survey and the ALMA wide-band sensitivity upgrade (J. Carpenter et al. 2023) will be pivotal in this endeavor.

Acknowledgments

We thank the anonymous referee for helpful comments and suggestions. We would like to thank Kazumasa Ohno and Satoshi Okuzumi for fruitful discussions on pebble accretion and Tomoya Hirota for helpful suggestions on masers. This Letter makes use of the following ALMA data: ADS/JAO.ALMA # 2023.1.00334.S, 2023.1.00525.S, and 2017.1.01687.S. ALMA is a partnership of ESO (representing its member states), NSF (USA), and NINS (Japan), together with NRC (Canada), NSTC and ASIAA (Taiwan), and KASI (Republic of Korea), in cooperation with the Republic of Chile. The Joint ALMA Observatory is operated by ESO, AUI/NRAO, and NAOJ. T.C.Y. was supported by the ALMA Japan Research Grant of NAOJ ALMA Project, NAOJ-ALMA-378. This work was supported by Grant-in-Aid for JSPS Fellows, JP23KJ1008 (T.C.Y.). F.A. and S.F. are funded by the European Union (ERC, UNVEIL, 101076613). Views and opinions expressed are, however, those of the authors only and do not necessarily reflect those of the European Union or the European Research Council. Neither the European Union nor the granting authority can be held responsible for them. S.F. also acknowledges financial contribution from PRIN-MUR 2022YP5ACE. G.R. acknowledges support from the European Union (ERC Starting Grant DiscEvol, project No. 101039651) and from Fondazione Cariplo, grant No. 2022-1217. Views and opinions expressed are, however, those of the author(s) only and do not necessarily reflect those of the European Union or the European Research Council. Neither the European Union nor the granting authority can be held responsible for them. Support for C.J.L. was provided by NASA through the NASA Hubble Fellowship grant No. HST-HF2-51535.001-A awarded by the Space Telescope Science Institute, which is operated by the Association of Universities for Research in Astronomy, Inc., for NASA, under contract NAS5-26555. M.B. has received funding from the European Research Council (ERC) under the European Union's Horizon 2020 research and innovation program (PROTOPLANETS, grant agreement No. 101002188). L.P. acknowledges support by the ANID BASAL project FB210003 and ANID FONDECYT Regular 1221442.

Facilities: ALMA.

Software: astropy(Astropy Collaboration et al. 2013, 2018, 2022), CASA(CASA Team et al. 2022).

Appendix A
Observational Details

We describe the observations and data reduction procedures here. The data were processed using the Common Astronomy Software Application Modular version 6.5 (CASA; CASA Team et al. 2022) as described below.

A.1. ^{28}SiS J = 16−15

The ^{28}SiS $J = 16-15$ line is located near the $H_2CO\ 4_{0,4}-3_{0,3}$ line and was observed as part of L. Trapman et al. (2025a; project ID: # 2023.1.00334.S; PI: L. Trapman). We used the data already reduced by them and summarized the main observational parameters here. Observations were performed between 2023 October and 2024 May in ALMA Band 7, with baseline lengths of 15–984 m. The on-source integration time was 34 minutes, and the velocity resolution was 1.2 km s^{-1}. Pipeline calibration and self-calibration were performed following R. A. Loomis et al. (2025). The continuum was subtracted in the visibility plane. We produced image cubes using the CLEAN algorithm with a pixel size of 0.″02 and two channel widths, $\Delta v = 1.25$ and 5.0 km s^{-1}, hereafter referred

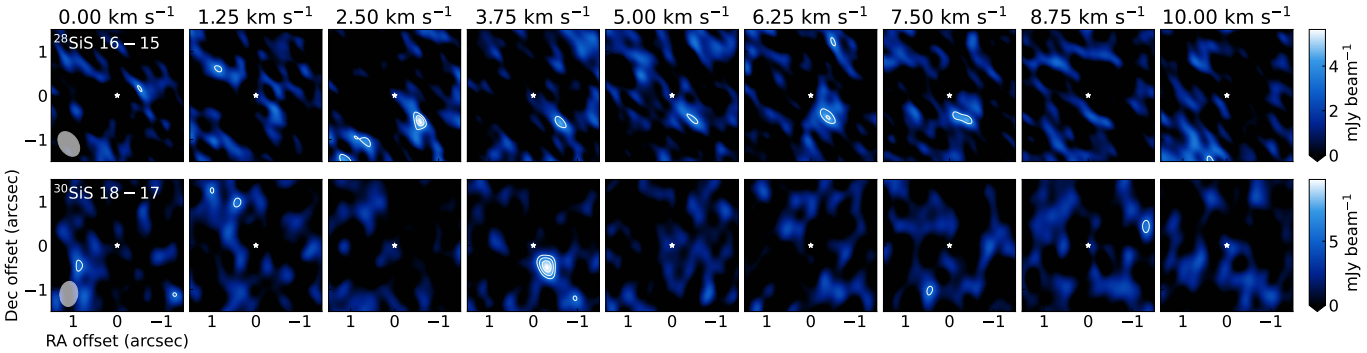

Figure 6. Channel maps of the ^{28}SiS $J = 16-15$ and ^{30}SiS $J = 18-17$ lines are shown. The cubes with narrow channel widths are plotted. The contours are drawn at [3, 4, 5]σ levels. Star symbols indicate the position of the central star. The gray ellipses show the synthesized beams.

to as narrow- and wide-channel cubes, respectively. The motivation for creating the wide-channel cube is to properly perform CLEAN by improving the S/N per channel for a more accurate flux estimate. Natural weighting, the Hogbom deconvolver, and a CLEAN threshold of 3σ (rms measured in line-free channels) were used. We did not apply a specific CLEAN mask but allowed the algorithm to construct CLEAN components for any signal above the threshold. The resultant beam size and rms for the narrow-channel cube were $\sim 0\farcs5$ and 1.1 mJy beam^{-1}, respectively (Table 1). The rms for the wide-channel cube was 0.85 mJy beam^{-1}.

A.2. ^{30}SiS J = 18−17

The ^{30}SiS $J = 18-17$ line was observed in ALMA Cycle 11 under project ID # 2023.1.00525.S (PI: T. Yoshida) in 2024 May, close in time to the second ^{28}SiS $J = 16-15$ execution. Baselines ranged from 15 to 741 m, with an on-source integration time of 48 minutes. The line was included in a spectral window primarily targeting the continuum, with a velocity resolution of ~ 0.9 km s^{-1}. Pipeline calibration included automatic self-calibration using the continuum image. Seven rounds of phase-only self-calibration were performed, improving the peak S/N from 330 to 1700 and producing a nearly Gaussian noise distribution. The continuum was subtracted in the visibility plane, and visibility cubes were generated. Image cubes were created using the same CLEAN procedure as for ^{28}SiS $J = 16-15$, but only with a velocity channel width of $\Delta v = 1.25$ km s^{-1}. The resulting beam size and rms are $\sim 0\farcs5$ and 1.7 mJy beam^{-1}, respectively (Table 1).

A.3. Channel Maps

Channel maps of the narrow-channel cubes for both ^{28}SiS $J = 16-15$ and ^{30}SiS $J = 18-17$ lines are shown in Figure 6. The star symbols indicate the position of the central star.

A.4. Histograms of the S/N Maps

Figure 7 presents the histograms of the background pixel values in the S/N maps (Figure 1). All pixels within a $10''$ square centered on the star were included, excluding the central $1''$ radius region that contains the signal. The histograms closely follow a Gaussian distribution and have no heavy tail, which is sometimes seen in an image with insufficient calibration. The detected signals are significantly above the background distribution.

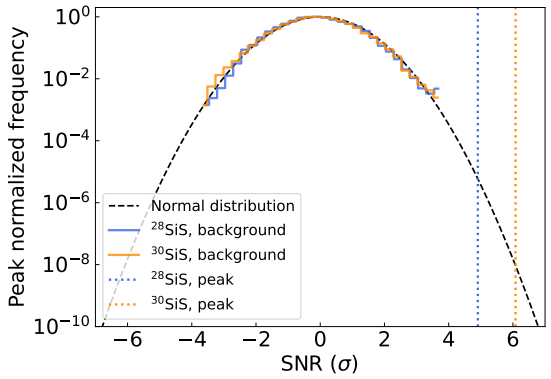

Figure 7. Histograms of the background pixel values of the S/N maps. The solid colored lines show the normalized histograms, while the dotted colored lines indicate the peak values corresponding to the detected signals. The black dashed line shows a normal distribution normalized to its peak, which matches the histograms well.

Appendix B
Caveats on Line Flux Modeling

To derive the physical quantities of SiS (Section 2.3), we assumed that the emission originates from a homogeneous slab and used the integrated fluxes. However, this assumption might be inadequate if the source has complex density, temperature, or velocity structures. Indeed, the line widths of the two isotopologues may differ (Figure 3); the ^{28}SiS $J = 16-15$ line has a width of ~ 5 km s^{-1}, while the ^{30}SiS $J = 18-17$ line is unresolved at a velocity resolution of ~ 1 km s^{-1}, although the current S/N of the ^{28}SiS $J = 16-15$ narrow-channel cube is not enough to conclude this. Furthermore, the peak intensity of the ^{30}SiS $J = 18-17$ line is about twice that of ^{28}SiS $J = 16-15$. This inversion may indicate a complex physical structure. For example, cold, optically thick ^{28}SiS could obscure a hot inner component, while ^{30}SiS, with lower optical depth, would allow the inner hot emission to emerge. We note that such an inverted temperature structure has been predicted for protoplanets (e.g., M. G. Brouwers et al. 2018).

Another caveat is the assumption of local thermal equilibrium. The critical density of the ^{28}SiS $J = 16-15$ line is $\sim 7 \times 10^7$ cm^{-3} according to the collisional rates in the LAMDA database (F. L. Schöier et al. 2005; J. Kłos & F. Lique 2008). We estimated the midplane gas density at $r = 60$ au based on the gas mass derived from CO and N_{2H}^+ emission (L. Trapman et al. 2025a, 2025b) and the characteristic radius from the rotation curve analysis (C. Longarini et al. 2025), using the parametric tapered power-law profile. The gas

surface density at $r = 60$ au is estimated to be $\Sigma_g \sim 5\,\mathrm{g\,cm^{-2}}$. The gas scale height is given by

$$H_g = \sqrt{\frac{k_\mathrm{B} T_\mathrm{mid}\, r^3}{\mu_\mathrm{gas} m_p G M_\star}} \simeq 3\ \mathrm{au}, \tag{B1}$$

where k_B, T_mid, μ_gas, m_p, and G are the Boltzmann constant, midplane temperature, mean molecular weight of the gas, proton mass, and gravitational constant, respectively. We adopt $\mu_\mathrm{gas} = 2.37$ and

$$T_\mathrm{mid} = \left(\frac{0.02 L_\star}{8\pi r^2 \sigma_\mathrm{SB}}\right)^{1/4} \simeq 17\ \mathrm{K}, \tag{B2}$$

where $L_\star = 1.2\,L_\odot$ (Á. Ribas et al. 2023) and σ_SB is the Stefan–Boltzmann constant, assuming that stellar irradiation sets the midplane temperature (e.g., J. Huang et al. 2018). The resulting midplane gas density is $n_{\mathrm{H_2}} \sim 1 \times 10^{10}\,\mathrm{cm^{-3}}$, two orders of magnitude higher than the critical density. Thus, the lines should be thermalized if collisional and spontaneous processes dominate the excitation.

Still, a possibility remains that the ^{30}SiS $J = 18-17$ emission is masing. The narrow line width and high peak flux could imply a maser, though they are also consistent with thermal broadening. ^{28}SiS masers are observed under similarly dense conditions around the carbon star IRC+10216 (J. P. Fonfría Expósito et al. 2006; Y. Gong et al. 2017), where infrared pumping due to overlapped lines between the ^{28}SiS rovibrational lines and other molecular lines such as C_2H_2 is a possible mechanism. This could be relevant for PDS 66 if a strong infrared source (e.g., a protoplanet) is present. However, the lack of collisional rate data and high-excitation spectroscopic data for ^{30}SiS $J = 18-17$ prevents detailed modeling.

Future high-resolution observations and detailed modeling would be valuable. Nevertheless, all the above scenarios are consistent, to varying degrees, with the presence of a local heating source and the sublimation of dust grains.

Appendix C
Comments on the Catalog Frequencies

We found that the ^{28}SiS $J = 16-15$ and ^{30}SiS $J = 18-17$ lines exhibit slightly different line-of-sight velocities. One possibility is that the gas velocities are intrinsically different, which could arise from complex physical structures along the line of sight (Appendix B).

Another possible explanation is an uncertainty in the spectroscopic data. In Figure 8, we show the spectra assuming the frequencies from the JPL database (H. M. Pickett et al. 1998) instead of those from the CDMS database (H. S. P. Müller et al. 2007). While the ^{28}SiS $J = 16-15$ line remains unchanged, the ^{30}SiS $J = 18-17$ line is redshifted by $\sim$3 km s^{-1} compared to the CDMS-based spectrum (Figure 3). Because this transition was not directly measured experimentally but predicted from other transitions in the catalogs, the spectroscopic parameters might carry some uncertainty. To test this, we refer to a spectral survey of the carbon star IRC+10216 by N. A. Patel et al. (2011), in which seven ^{30}SiS transitions, including ^{30}SiS $J = 18-17$, between 294–350 GHz were detected with the Submillimeter Array. They measured the line frequencies and compared them to the CDMS database. Among these lines, ^{30}SiS $J = 18-17$ shows the largest blueshift, $\sim$1 MHz (or $\sim$1 km s^{-1}), from the mean value, although the scatter is considerable. This supports the possibility that the CDMS frequency for ^{30}SiS $J = 18-17$ might be slightly overestimated. Future laboratory measurements are required to confirm this.

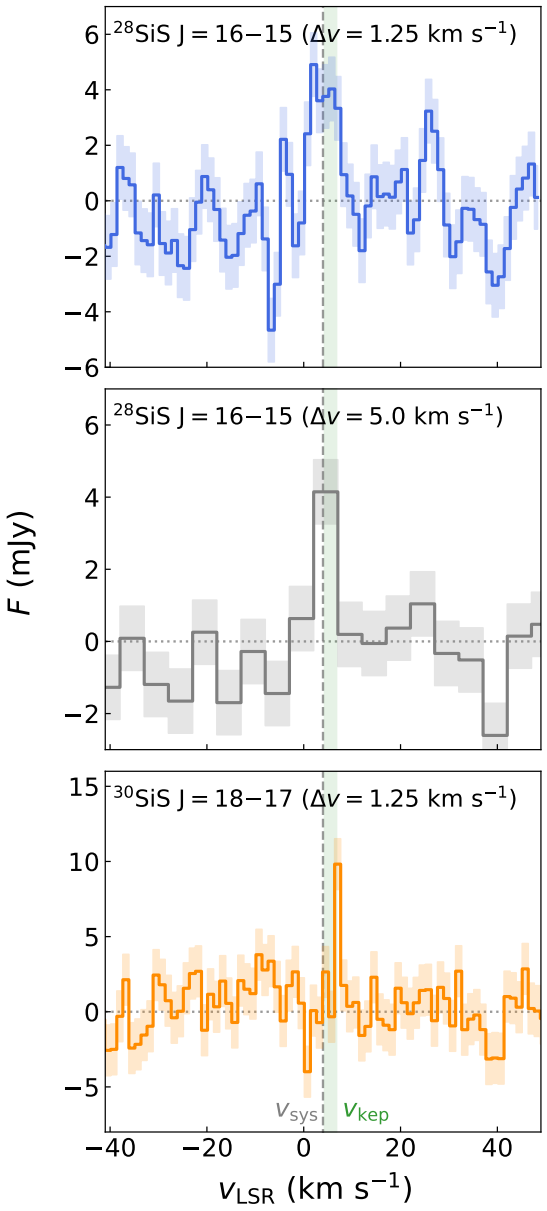

Figure 8. Spectra of the SiS lines assuming the JPL database frequencies.

ORCID iDs

Tomohiro C. Yoshida https://orcid.org/0000-0001-8002-8473
Felipe Alarcón https://orcid.org/0000-0002-2692-7862
Jaehan Bae https://orcid.org/0000-0001-7258-770X
Myriam Benisty https://orcid.org/0000-0002-7695-7605
Kiyoaki Doi https://orcid.org/0000-0003-1958-6673
Stefano Facchini https://orcid.org/0000-0003-4689-2684
Charles J. Law https://orcid.org/0000-0003-1413-1776
Hideko Nomura https://orcid.org/0000-0002-7058-7682
Laura Perez https://orcid.org/0000-0002-1199-9564
Giovanni Rosotti https://orcid.org/0000-0003-4853-5736
Yuhito Shibaike https://orcid.org/0000-0003-2993-5312

Richard Teague https://orcid.org/0000-0003-1534-5186
Takashi Tsukagoshi https://orcid.org/0000-0002-6034-2892
Yoshihide Yamato https://orcid.org/0000-0003-4099-6941

References

Aguayo, A., Caceres, C., Guo, Z., et al. 2025, A&A, 698, A165
Alarcón, F., Bergin, E. A., & Teague, R. 2022, ApJL, 941, L24
Andrews, S. M., Huang, J., Pérez, L. M., et al. 2018, ApJL, 869, L41
Asplund, M., Amarsi, A. M., & Grevesse, N. 2021, A&A, 653, A141
Astropy Collaboration, Price-Whelan, A. M., Lim, P. L., et al. 2022, ApJ, 935, 167
Astropy Collaboration, Price-Whelan, A. M., Sipőcz, B. M., et al. 2018, AJ, 156, 123
Astropy Collaboration, Robitaille, T. P., Tollerud, E. J., et al. 2013, A&A, 558, A33
Avenhaus, H., Quanz, S. P., Garufi, A., et al. 2018, ApJ, 863, 44
Bae, J., Hartmann, L., Zhu, Z., & Nelson, R. P. 2014, ApJ, 795, 61
Bae, J., Isella, A., Zhu, Z., et al. 2023, ASPC, 534, 423
Bae, J., Teague, R., Andrews, S. M., et al. 2022, ApJL, 934, L20
Benisty, M., Bae, J., Facchini, S., et al. 2021, ApJL, 916, L2
Bergin, E. A., Du, F., Cleeves, L. I., et al. 2016, ApJ, 831, 101
Birnstiel, T., Dullemond, C. P., Zhu, Z., et al. 2018, ApJL, 869, L45
Booth, A. S., Calahan, J., Temmink, M., et al. 2025, AJ, 171, 128
Booth, A. S., Ilee, J. D., Walsh, C., et al. 2023, A&A, 669, A53
Bosman, A. D., Alarcón, F., Bergin, E. A., et al. 2021, ApJS, 257, 7
Brouwers, M. G., Vazan, A., & Ormel, C. W. 2018, A&A, 611, A65
Carpenter, J., Brogan, C., Iono, D., & Mroczkowski, T. 2023, in Physics and Chemistry of Star Formation: The Dynamical ISM across Time and Spatial Scales, ed. V. Ossenkopf-Okada et al., 304
CASA Team, Bean, B., Bhatnagar, S., et al. 2022, PASP, 134, 114501
Cherchneff, I. 2006, A&A, 456, 1001
Cleeves, L. I., Bergin, E. A., & Harries, T. J. 2015, ApJ, 807, 2
Cortes, P., Carpenter, J., Kameno, S., et al. 2025, ALMA Cycle 12 Technical Handbook v1.0, Zenodo, doi:10.5281/zenodo.14933753
Cridland, A. J., Lega, E., & Benisty, M. 2025, A&A, 693, A86
Curone, P. 2025, exoALMA IV. Data Products, v1, Harvard Dataverse
Curone, P., Facchini, S., Andrews, S. M., et al. 2025, ApJL, 984, L9
Danilovich, T., Richards, A. M. S., Karakas, A. I., et al. 2019, MNRAS, 484, 494
Danilovich, T., Samaratunge, N., Mori, Y., et al. 2025, A&A, 704, A341
Dong, R., & Fung, J. 2017, ApJ, 835, 146
Drążkowska, J., Bitsch, B., Lambrechts, M., et al. 2023, ASPC, 534, 717
Fonfría Expósito, J. P., Agúndez, M., Tercero, B., Pardo, J. R., & Cernicharo, J. 2006, ApJL, 646, L127
Fortenberry, R. C., & McGuire, B. A. 2024, ApJ, 971, 101
Gaia Collaboration, Brown, A. G. A., Vallenari, A., et al. 2021, A&A, 649, A1
Galloway-Sprietsma, M., Bae, J., Izquierdo, A. F., et al. 2025, ApJL, 984, L10
Ginsburg, A., McGuire, B. A., Sanhueza, P., et al. 2023, ApJ, 942, 66
Gong, Y., Henkel, C., Ott, J., et al. 2017, ApJ, 843, 54
Gusdorf, A., Pineau Des Forêts, G., Cabrit, S., & Flower, D. R. 2008, A&A, 490, 695
Haffert, S. Y., Bohn, A. J., de Boer, J., et al. 2019, NatAs, 3, 749
Hammond, I., Christiaens, V., Price, D. J., et al. 2023, MNRAS, 522, L51
Huang, J., Andrews, S. M., Dullemond, C. P., et al. 2018, ApJL, 869, L42
Ingleby, L., Calvet, N., Herczeg, G., et al. 2013, ApJ, 767, 112
Izquierdo, A. F., Stadler, J., Galloway-Sprietsma, M., et al. 2025, ApJL, 984, L8
Jennings, J., Booth, R. A., Tazzari, M., Rosotti, G. P., & Clarke, C. J. 2020, MNRAS, 495, 3209
Keppler, M., Benisty, M., Müller, A., et al. 2018, A&A, 617, A44
Keyte, L., Kama, M., Booth, A. S., Law, C. J., & Leemker, M. 2024, MNRAS, 534, 3576
Kłos, J., & Lique, F. 2008, MNRAS, 390, 239
Krijt, S., Bosman, A. D., Zhang, K., et al. 2020, ApJ, 899, 134
Lambrechts, M., & Johansen, A. 2012, A&A, 544, A32
Law, C. J., Booth, A. S., & Öberg, K. I. 2023, ApJL, 952, L19
Lock, S. J., & Stewart, S. T. 2017, JGRE, 122, 950
Longarini, C., Lodato, G., Rosotti, G., et al. 2025, ApJL, 984, L17
Loomis, R. A., Facchini, S., Benisty, M., et al. 2025, ApJL, 984, L7
Lovas, F. J., & Tiemann, E. 1974, JPCRD, 3, 609
Madhusudhan, N., Bitsch, B., Johansen, A., & Eriksson, L. 2017, MNRAS, 469, 4102
Mamajek, E. E., Meyer, M. R., & Liebert, J. 2002, AJ, 124, 1670
McClure, M. K., van't Hoff, M., Francis, L., et al. 2025, Natur, 643, 649
Mendoza, E., Costa, S. F. M., Carvajal, M., et al. 2024, A&A, 687, A149
Miotello, A., Kamp, I., Birnstiel, T., Cleeves, L. C., & Kataoka, A. 2023, ASPC, 534, 501
Mota, V. C., Varandas, A. J. C., Mendoza, E., Wakelam, V., & Galvão, B. R. L. 2021, ApJ, 920, 37
Müller, H. S. P., McCarthy, M. C., Bizzocchi, L., et al. 2007, PCCP, 9, 1579
Müller, H. S. P., Schlöder, F., Stutzki, J., & Winnewisser, G. 2005, JMoSt, 742, 215
Öberg, K. I., Murray-Clay, R., & Bergin, E. A. 2011, ApJL, 743, L16
Ormel, C. W. 2024, arXiv:2411.14643
Ormel, C. W., & Klahr, H. H. 2010, A&A, 520, A43
Paiva, M. A. M., Lefloch, B., & Galvão, B. R. L. 2020, MNRAS, 493, 299
Patel, N. A., Young, K. H., Gottlieb, C. A., et al. 2011, ApJS, 193, 17
Pickett, H. M., Poynter, R. L., Cohen, E. A., et al. 1998, JQSRT, 60, 883
Pinte, C., Ilee, J. D., Huang, J., et al. 2025, ApJL, 984, L15
Pinte, C., Price, D. J., Ménard, F., et al. 2018, ApJL, 860, L13
Podio, L., Codella, C., Lefloch, B., et al. 2017, MNRAS, 470, L16
Pollack, J. B., Hollenbach, D., Beckwith, S., et al. 1994, ApJ, 421, 615
Quillen, A. C., & Trilling, D. E. 1998, ApJ, 508, 707
Ribas, Á., Macías, E., Weber, P., et al. 2023, A&A, 673, A77
Ribas, Á., Vioque, M., Zagaria, F., et al. 2025, NatAs, 9, 1176
Rosi, M., Mancini, L., Skouteris, D., et al. 2018, CPL, 695, 87
Schöier, F. L., Bast, J., Olofsson, H., & Lindqvist, M. 2007, A&A, 473, 871
Schöier, F. L., van der Tak, F. F. S., van Dishoeck, E. F., & Black, J. H. 2005, A&A, 432, 369
Shibaike, Y., & Mordasini, C. 2024, A&A, 687, A166
Steinmeyer, M.-L., & Johansen, A. 2024, A&A, 683, A217
Steinmeyer, M.-L., Woitke, P., & Johansen, A. 2023, A&A, 677, A181
Szulágyi, J., Masset, F., Lega, E., et al. 2016, MNRAS, 460, 2853
Tanaka, K. E. I., Zhang, Y., Hirota, T., et al. 2020, ApJL, 900, L2
Teague, R., Bae, J., & Bergin, E. A. 2019, Natur, 574, 378
Teague, R., Benisty, M., Facchini, S., et al. 2025, ApJL, 984, L6
Tercero, B., Vincent, L., Cernicharo, J., Viti, S., & Marcelino, N. 2011, A&A, 528, A26
Testi, L., Birnstiel, T., Ricci, L., et al. 2014, in Protostars and Planets VI, ed. H. Beuther et al. (Univ. Arizona Press), 339
Trapman, L., Longarini, C., Rosotti, G. P., et al. 2025a, ApJL, 984, L18
Trapman, L., Zhang, K., Rosotti, G. P., et al. 2025b, ApJ, 989, 5
Valletta, C., & Helled, R. 2019, ApJ, 871, 127
Wang, Y., Ormel, C. W., Huang, P., & Kuiper, R. 2023, MNRAS, 523, 6186
Wolff, S. G., Perrin, M., Millar-Blanchaer, M. A., et al. 2016, ApJL, 818, L15
Yoshida, T. C., Nomura, H., Law, C. J., et al. 2024, ApJL, 971, L15
Youdin, A. N., & Goodman, J. 2005, ApJ, 620, 459
Zagaria, F., Jiang, H., Cataldi, G., et al. 2025, ApJ, 989, 30
Zanchet, A., Roncero, O., Agúndez, M., & Cernicharo, J. 2018, ApJ, 862, 38